The Astrophysical Journal, 943:33 (14pp), 2023 January 20 https://doi.org/10.3847/1538-4357/aca894

Small-scale Magnetic Flux Ropes in Stream Interaction Regions from Parker Solar Probe and Wind Spacecraft Observations

Yu Chen[1], Qiang Hu[1,2], Robert C. Allen[3], and Lan K. Jian[4]
[1] Center for Space Plasma and Aeronomic Research (CSPAR), The University of Alabama in Huntsville, Huntsville, AL 35805, USA; qh0001@uah.edu
[2] Department of Space Science, The University of Alabama in Huntsville, Huntsville, AL 35805, USA
[3] Johns Hopkins University Applied Physics Laboratory, Laurel, MD 20723, USA
[4] Heliophysics Science Division, NASA Goddard Space Flight Center, Greenbelt, MD 20771, USA
Received 2022 August 18; revised 2022 November 30; accepted 2022 December 1; published 2023 January 23

Abstract

Using in situ measurements from the Parker Solar Probe and Wind spacecraft, we investigate the small-scale magnetic flux ropes (SFRs) and their properties inside stream interaction regions (SIRs). Within SIRs from ∼0.15 to 1 au, SFRs are found to exist in a wide range of solar wind speeds with more frequent occurrences after the stream interface, and the Alfvénicity of these structures decreases significantly with increasing heliocentric distances. Furthermore, we examine the variation of five corresponding SIRs from the same solar sources. The enhancements of suprathermal electrons within these SIRs persist at 1 au and are observed multiple times. An SFR appears to occur repeatedly with the recurring SIRs and is traversed by the Wind spacecraft at least twice. This set of SFRs has similarities in variations of the magnetic field components, plasma bulk properties, density ratio of solar wind alpha and proton particles, and unidirectional suprathermal electrons. We also show, through the detailed time-series plots and Grad–Shafranov reconstruction results, that they possess the same chirality and carry comparable amounts of magnetic flux. Lastly, we discuss the possibility for these recurring SFRs to be formed via interchange reconnection, maintain the connection with the Sun, and survive up to 1 au.

Unified Astronomy Thesaurus concepts: Solar wind (1534); Fast solar wind (1872); Astronomy data analysis (1858); Solar magnetic reconnection (1504)

1. Introduction

Small-scale magnetic flux ropes (hereafter, SFRs), which consist of twisted magnetic field lines, have a much shorter duration and smaller cross-sectional dimension than magnetic clouds (Moldwin et al. 2000). During the past two decades, SFRs have been detected in abundance at various heliocentric distances (Cartwright & Moldwin 2010; Chen & Hu 2020), in different forms (Borovsky 2008; Yu et al. 2014), and by using different data analysis techniques (Hu et al. 2018; Pecora et al. 2021; Zhao et al. 2021) from in situ spacecraft measurements in the solar wind.

These small-scale structures have been suggested to have multiple sources. They can be created locally together with intermittent current sheets via the magnetohydrodynamic (MHD) turbulence (Greco et al. 2009; Zank et al. 2014; Zheng & Hu 2018). For example, the observational results by Zheng & Hu (2018), which reveal similar waiting time distributions and non-Gaussian distribution of the axial current density as the MHD turbulence simulation results, further support such a mechanism. On the other hand, SFRs are also believed to have a direct connection to the Sun. Some events observed at 1 au were traced back to the solar surface, such as the coronal sector boundaries and surrounding regions near the Sun (Kilpua et al. 2009). Some could also be a part of a coronal mass ejection, with the spacecraft only traversing a perimeter area (Rouillard et al. 2011). Away from the solar surface at heliocentric distances $\gtrsim$0.13 au, SFRs were found to occur frequently. Among those identified events, some overlap with magnetic switchbacks based on the latest in situ measurements from the Parker Solar Probe (PSP; Chen et al. 2021; Chen & Hu 2022). In the meantime, the interchange reconnection in the low corona was proposed as one of the generation mechanisms (Drake et al. 2021).

Notice that the rotation of the magnetic field is not a unique feature of SFRs, and also exists in other structures, such as torsional Alfvén waves, Alfvén vortices, and magnetic switchbacks. These other types of structures can occur or be recognized simultaneously with SFRs, and all possess the characteristics of significant field-aligned flow, hence being more dynamic. The internal process, e.g., the evolution of thermodynamics, may differ between quasi-static SFRs and those dynamic structures (Teh 2021). But neither the macroscopic properties, such as the scale size and duration, nor the 2D magnetic configurations exhibit substantial differences (Chen et al. 2021). A quasi-static SFR may also be able to evolve to be a dynamic structure through certain processes, e.g., the coalescence of multiple SFRs through magnetic reconnection (Agapitov et al. 2022).

SFRs sometimes occur in conjunction with other solar wind structures. For example, they have been discovered to occur in the vicinity of heliospheric current sheets (HCSs) based on single-point in situ measurements (Moldwin et al. 1995; Hu et al. 2018). Another type of large-scale structure, the stream interaction regions (SIRs) are defined as the region where the fast-speed solar wind expands into the preceding slow-speed solar wind. SIRs are also called corotating interaction regions (CIRs) when some of them recur for more than one solar rotation and appear to be corotating with the Sun. The interaction of the two different-speed streams causes the total pressure, i.e., the sum of the plasma pressure and the magnetic pressure, to reach its maximum that also defines the stream

interface (Smith & Wolfe 1976; Jian et al. 2006) sometimes. Additional characteristics include decreased proton number density and increased temperature across a stream interface. Multipoint observations reveal that an SIR can be a long-lasting structure, whose signatures can vary radially and longitudinally (Jian et al. 2009, 2019). Recently, the identification of SIRs was extended further into the inner heliosphere (Allen et al. 2020; Cohen et al. 2020), through the in situ measurements of the PSP.

Statistics of SFRs in SIRs at 1 au have been analyzed by Xu et al. (2020), based on the list of SIRs from Jian et al. (2006, 2013), Chi et al. (2018). They also compared the SFRs in the interplanetary coronal mass ejections (ICMEs) and the background solar wind. These small-scale structures in SIRs are found to be distinct from those in ICMEs, such as the lack of enhanced field strength and apparent expansion. However, whether SFRs in SIRs in the inner heliosphere (<1 au) have different properties from those in the ambient solar wind is still unknown. Moreover, even if SFRs with magnetic field lines rooted on the solar surface can be detected in the interplanetary space at one point, it is still not clear how they evolve. The variations and evolution with heliocentric distances and heliographic latitudes have been mostly studied through statistical analyses of multispacecraft data sets individually (e.g., Chen et al. 2019; Chen & Hu 2020). Tracking an individual SFR over certain heliocentric distances for case studies is not easy because (1) the structure is small in comparison to the separation distance between two or more spacecraft, and (2) one-to-one correspondence between different points of measurements is hard to establish due to uncertainties. For large-scale SIRs, Allen et al. (2021) found a number of recurring events that last for several solar rotations and thus observed by one or more spacecraft repeatedly. These SIRs represent the slow and fast-speed solar wind streams that travel to 1 au from the same solar sources, allowing us to investigate the temporal and possibly radial evolution of SFRs embedded within these corresponding events in both a statistical and a case-by-case manner.

In this paper, we use the in situ measurements from two spacecraft, namely the PSP and Wind spacecraft, to analyze the evolution of the solar wind and the SFR properties inside SIRs from the PSP orbits (heliocentric distances as low as ~0.15 au) to 1 au. The identification of SFR has been generalized recently to allow for SFR configurations with and without significant field-aligned flow as compared with the local Alfvén velocity (Chen et al. 2021). The latter is sometimes classified as static SFRs. Therefore, the term *SFR* in this work is defined in a broad sense, including both quasi-static SFR and flux rope structure with significant plasma flow aligned with the local magnetic field, as viewed in a proper frame of reference moving with the structure. Also, we mostly adopt the terminology *SIR* without further distinguishing it from CIR since our focus is mainly on the structure and the associated SFRs inside.

This paper is organized as follows. In Section 2, we briefly describe the method of SFR identification and the criteria for selecting SIRs and determining their stream interfaces as well as the introduction of spacecraft data sets. In Section 3, we present superposed epoch analysis of selected SIRs and SFRs properties within these SIRs for both PSP and Wind events. We also study the evolution of some SFR properties, such as the Alfvénicity, from the inner heliosphere to 1 au. In addition, we show time-series variations for five corresponding SIRs that were observed by both spacecraft in Section 4. A recurring SFR that is possibly traversed by the Wind spacecraft several times is also presented in this section. We provide a summary of the related SFR parameters together with detailed time-series plots, and the Grad–Shafranov (GS)-type reconstruction results. We also compare the magnetic field variations of the recurring SFR with the corresponding intervals inside the PSP SIR event. Finally, in Section 5, we summarize our primary findings and propose future work.

2. Method and Data

In this study, SIRs identified via the Wind spacecraft data and those in PSP encounters (E1)–(E5) are adopted from Allen et al. (2021), whereas those in PSP (E6)–(E9) are from the live catalog on the PSP Science Gateway at https://sppgway.jhuapl.edu/Event_List. Only events with (1) publicly available data and (2) a clearly recognized stream interface are included in this analysis. Totally, there are 13 SIRs identified via the PSP and 12 via the Wind spacecraft data, respectively.

The stream interface in Allen et al. (2021) is determined by the maximum of the total pressure $P_{\max}$, where $P = n_p k T_p + B^2/2\mu_0$, and n_p and T_p are proton number density and temperature, respectively. Since both electron and alpha particles data of the PSP are now available, we recalculate the total pressure via $P = \sum_i n_i k T_i + B^2/2\mu_0$, where $i = p,\ e,\ He$, corresponding to the parameters of proton, electron, and alpha particles. Notice that the proton data in the PSP SIRs have rather good data integrity, while the electron and alpha particles parameters sometimes have data gaps or are unavailable for the whole interval. These data issues will lead to uncertainties of $P_{\max}$. Thus, it is necessary to consider additional criteria when reexamining the stream interface. According to Crooker et al. (1999), the primary signatures of the stream interface include "a drop in number density, a rise in temperature, and a flow shear." The change in the solar wind alpha-to-proton number density ratio will also be taken into account when n_{He} is available. These three or four criteria sometimes result in several candidates for the stream interface. In such a case, we select the one that is closest to the $P_{\max}$. Reexamination of the stream interfaces of the Wind SIRs also follows the above procedure.

We implemented the extended GS-based detection algorithm to generate the flux rope event list, which is the same as the technique reported in Chen & Hu (2022). It is carried out for the time periods around the dates when those SIRs are identified and up to the PSP (E9) in 2021 August. This method is able to automatically identify the cylindrical structure ($\partial/\partial z = 0$ along the z-axis) of SFR characterized by the double-folding pattern of the physical quantities P_t versus A along the spacecraft path in its original implementation (Sonnerup & Guo 1996; Hau & Sonnerup 1999; Hu & Sonnerup 2002; Hu et al. 2018). Here, P_t is the transverse pressure, i.e., the sum of the thermal pressure and the axial magnetic pressure $P_t = p + B_z^2/2\mu_0$, and A is the magnetic flux function in 2D. In an extended algorithm, such a relationship is sought for modified quantities P_t' and A'. In the extended GS equation (Teh 2018),

$$\nabla^2 A' = -\mu_0 \frac{d}{dA'}\left[(1-\alpha)^2 \frac{B_z^2}{2\mu_0} + (1-\alpha)p + \alpha(1-\alpha)\frac{B^2}{2\mu_0}\right]; \quad (1)$$

these two quantities are $A' = (1 - \alpha)A$, and $P_t' = [...]$. The latter consists of three pressure terms within the brackets. The parameter α is the square of the average Alfvén Mach number, i.e., $\langle M_A \rangle^2$, which is approximately a constant. For $\alpha \equiv 0$, the Equation (1) reduces to the original GS equation. The aforementioned double-folding pattern in the extended GS-based detection applies to P_t' versus A', which is examined along the spacecraft path between two branches separated by the extremum value of the magnetic flux function A. An SFR record will have to possess a good double-folding pattern and be able to satisfy a set of criteria, as listed in Chen & Hu (2022). Detailed descriptions of the theoretical basis and the implementation of the GS-based algorithm are provided by Hu et al. (2018), and an online flowchart is available at http://www.fluxrope.info/flowchart.html.

In addition, one should notice that the thermal pressure p in Equation (1) only considers the proton number density and temperature due to data issues. There are 4 out of 13 PSP SIRs that do not have electron data during the whole interval, and 5 SIRs have some gaps that will cause discontinuous P_t'. Only 5 PSP SIRs have alpha particle data. Therefore, we cannot include the electron and alpha particles data in the GS detection based on the PSP data set because they do not have continuous data coverage. To be consistent, the GS detection via the Wind data set uses the same calculation of P_t'. Usually the GS-based detection and the GS reconstruction are two independent processes. For the former, based on data availability and our prior experience, only the magnetic field measurements can be applied for continuous detection, corresponding to part of the terms inside the brackets of the right-hand side of Equation (1). For the latter, all the terms are included to solve the GS Equation (1).

The measurements of the magnetic field and solar wind bulk properties from the PSP are provided by two instrument suites on board: the FIELDS (Bale et al. 2016) and the Solar Wind Electrons Alphas and Protons (Kasper et al. 2016), respectively. The number density and temperature of electron and alpha particles are respectively from the FIELDS Simplified Quasi-Thermal Noise data (Moncuquet et al. 2020) and the Solar Probe Analyzers Ion (SPAN-Ion; Livi et al. 2022). The proton data from the Solar Probe Cup (SPC; Case et al. 2020) are mainly used, and the SPAN-Ion data will be considered when the SPC data are unavailable. Notice that the proton parameters are provided with significant uncertainties via the SPAN-ion instrument as indicated in some studies (e.g., Finley et al. 2021). In the detection using the SPAN-Ion data, we choose to omit the thermal pressure in the expression of the modified transverse pressure P_t' and instead rely on the two magnetic pressure-related terms (see Equation (1)). In this study, we also show the electron pitch angle distribution (ePAD) data, which are provided by the SPAN-Electron instrument (Whittlesey et al. 2020). All data from the PSP in situ measurements are downsampled to a cadence of 28 s.

The data at 1 au are from the Wind spacecraft measurements. The magnetic field, plasma bulk properties, and the ePAD data are provided by the Magnetic Field Investigation (Lepping et al. 1995), the Solar Wind Experiment (Ogilvie et al. 1995), and 3D Plasma and Particle Investigation (Lin et al. 1995) respectively. All data are processed to a resolution of 1 minute.

3. Statistical Analysis

As introduced in the previous section, we extend the GS-based detection to time periods that cover the SIRs–CIRs given in Allen et al. (2021; from PSP (E1) to (E5)) and an updated event list (up to (E9)) as well as those during the corresponding events observed by the Wind spacecraft. The start and end times of selected SIRs are listed in Table 1. The times of adjusted stream interfaces that separate the low- and high-speed solar wind are shown in the fourth column, which are determined by following the procedure as introduced in Section 2. Among these 25 events, the first 13 are identified from the PSP spacecraft data, with the rest coming from the Wind observation. The fifth column shows the duration in minutes of the SIR intervals, and the numbers of identified SFRs within the corresponding SIRs are listed in the last column.

In these SIRs, there are 88 SFRs with durations ranging from 4 minutes to 1 hr identified with the PSP data. Inside the SIRs, these occurrences are scattered in random numbers, ranging from 1 to 18. Based on the separation of the slow and fast solar wind streams, 31 SFRs are upstream (before the stream interface), and 57 are downstream (after the stream interface). Notice that the SFR event counts appear unevenly in each SIR period. This is due to the fact that SIR intervals vary in length (see Table 1), and the stream interfaces are not located in the middle of each interval.

The SIR identification at Lagrange point L1 was carried out based on ACE and Wind spacecraft measurements. Due to the data integrity issue, we solely focus on the SFR detection via the Wind spacecraft. A total of 168 SFRs were discovered inside 12 identified SIRs. Forty-six out of them are upstream, whereas the remaining 122 are downstream. The count of SFR at 1 au is about twice the number at PSP. Since the SIR intervals are generally longer at 1 au, we calculate the event rate per hour for both detection results. The PSP and Wind SIRs have the SFR hourly occurrence rates of 0.9 and 1.33 (after taking data integrity issue into account), respectively. The disparity in counts could be the consequence of additional SFRs generated from the local source at 1 au.

As an example, Figure 1 shows a summary of one SIR event included in the Table 1, namely, no. (4). The time-series plot runs from 2019 August 24, 04:00 to 18:00 UT, covering both ends of the SIR event from 06:00 to 15:30 UT (two black vertical dashed lines). Variables on the left and right y-axes are indicated by black and blue curves, respectively. During this time period, 18 SFRs have been detected, which are enclosed by gray shaded areas. These SFRs have an average duration of 12 minutes and an average scale size of 0.0016 au. The first three panels present the magnetic field and the solar wind velocity in the radial, tangential, and normal (RTN) coordinates. Within the SIR interval, the principal component of solar wind velocity V_R increases from ~325 to 425 km s^{-1}. The bipolar rotation of the magnetic field that helps determine the signature of an SFR is sometimes not induced by a single component. In the longest SFR interval around 12:00 UT, for example, two magnetic field components varying from negative to positive values can be clearly seen. It is noteworthy that the GS-based algorithm can also detect SFRs with relatively weak rotation in addition to those with strong rotations of the magnetic field. Apart from the field rotation, the velocity rotates with the magnetic field as well in some cases, resulting in a structure with high Alfvénicity. The degree of the

Table 1
SIRs and SFRs from the PSP and Wind Observations

#[a]	Start Time (UT)	End Time (UT)	Time of Max Pressure (UT)	Duration (minutes)	Count of SFRs
1	2018 Nov 14 20:40:00	2018 Nov 15 07:25:00	2018 Nov 14 23:06:00	646	2
2	2019 Apr 6 20:20:00	2019 Apr 7 01:25:00	2019 Apr 6 21:55:30	306	4
3	2019 Aug 22 22:00:00	2019 Aug 23 04:40:00	2019 Aug 22 22:36:08	401	10
4	2019 Aug 24 06:00:00	2019 Aug 24 15:30:00	2019 Aug 24 08:30:48	571	18
5	2019 Aug 26 04:55:00	2019 Aug 26 11:50:00	2019 Aug 26 07:16:24	416	10
6	2019 Aug 29 05:30:00	2019 Aug 29 13:50:00	2019 Aug 29 07:25:40	501	13
7	2020 May 19 09:04:00	2020 May 19 15:48:00	2020 May 19 11:38:16	405	1
8	2020 Aug 25 09:20:00	2020 Aug 26 04:20:00	2020 Aug 25 14:26:16	1141	2
9	2020 Sep 21 23:30:00	2020 Sep 22 04:50:00	2020 Sep 22 01:51:30	321	5
10	2021 Jan 12 14:05:00	2021 Jan 12 19:30:00	2021 Jan 12 15:58:40	326	13
11	2021 Apr 24 21:40:00	2021 Apr 25 01:30:00	2021 Apr 25 00:05:30	231	4
12	2021 Apr 26 18:20:00	2021 Apr 27 02:00:00	2021 Apr 26 21:19:04	461	1
13	2021 Aug 6 02:20:00	2021 Aug 6 06:30:00	2021 Aug 6 04:57:24	251	5
14	2018 Aug 14 22:00:00	2018 Aug 16 00:10:00	2018 Aug 15 07:09:00	131	13
15	2018 Aug 19 16:20:00	2018 Aug 20 08:40:00	2018 Aug 20 02:49:00	981	11
16	2018 Sep 10 09:50:00	2018 Sep 11 12:20:00	2018 Sep 10 21:39:30	151	17
17	2018 Sep 16 23:30:00	2018 Sep 17 18:10:00	2018 Sep 17 05:55:00	1121	20
18	2018 Oct 7 07:30:00	2018 Oct 7 21:20:00	2018 Oct 7 13:31:00	831	4
19	2018 Oct 13 08:00:00	2018 Oct 14 16:20:00	2018 Oct 13 18:08:00	501	17
20	2018 Nov 4 14:30:00	2018 Nov 5 06:00:00	2018 Nov 4 22:27:00	931	11
21	2018 Nov 9 12:00:00	2018 Nov 10 15:40:00	2018 Nov 9 21:49:00	221	12
22	2019 Jul 8 17:00:00	2019 Jul 10 07:50:00	2019 Jul 8 23:11:00	891	26
23	2019 Aug 4 23:00:00	2019 Aug 5 21:00:00	2019 Aug 5 02:52:00	1321	12
24	2019 Aug 30 08:25:00	2019 Aug 31 13:10:00	2019 Aug 30 17:18:00	286	18
25	2019 Sep 27 05:00:00	2019 Sep 27 22:40:00	2019 Sep 27 11:32:00	1061	7

Note.
[a] Events nos. (1)–(13) and nos. (14)–(25) are identified by the PSP and Wind spacecraft, respectively.

Alfvénicity is quantified by the value of the Walén test slope, i.e., the slope of the linear regression line between the remaining flow and the local Alfvén velocities. It varies from 0.008 to 0.81 for the SFRs identified during this time period, corresponding to both static and Alfvénic structures. The fourth panel depicts the field strength and the solar wind speed. The magnitude of the magnetic field reaches its maximum at the stream interface (vertical red dashed line), and the speed significantly increases after it. The corresponding flow angles V_θ and V_ϕ (in RTN) are presented in the fifth panel, which shows deflections of flow direction at the stream interface. The sixth and seventh panels display the temperature and number density of proton and electron, denoted by T_p, T_e, n_p, and n_e. The T_p, n_p, and n_e exhibit opposite trends of change during the entire time period due to increasing solar wind speed, while T_e remains nearly unchanged. In contrast to the SIR interval, there is no consistent variation in temperature or number density throughout the SFRs. Here, we only display the proton β due to discontinuous electron number density. The aforementioned tendencies in T_p and n_p lead some SFRs to have low proton β_p, while others have β_p values close to unity. The eighth panel shows two versions of the total pressure, denoted by $P_{B,p}$ and $P_{B,p,e}$, where subscripts B, p, e represent the contributions from the magnetic field, protons, and electrons, respectively. Since the electron data are discontinuous, it is uncertain where the maximum $P_{B,p,e}$ locates. The total pressure $P_{B,p}$ reaches its maximum at 08:37:30, which is close to the stream interface, i.e., at 08:30:48 (see Table 1). The last panel shows the pitch angle distribution of suprathermal electrons (at 315 eV). The unidirectional electron strahl exists for most of the time, except for some time periods, e.g., near 15:00 UT where the electrons are bidirectional. Such counterstreaming suprathermal electrons may likely indicate that the magnetic field lines are rooted on the Sun with both ends (Gosling 1990).

Figure 2 presents the overview of SIRs and SFRs detected via the PSP (top) and Wind (bottom) data sets. The solar wind speed of each event is depicted in the left panels, all centered around the time of the stream interface (0 hr). The temporal span for the PSP results is [−8, 8] hr with the stream interface at 0 hr (see Figure 2(a)). Although all events have a range of low to intermediate solar wind speeds, there is an apparent transition from upstream to downstream $V_{\rm SW}$, with speeds rising approximately from (200, 400) to (300, 570) km s^{-1}. The black curve represents the average $V_{\rm SW}$ for all PSP SIRs listed in Table 1. This speed increases by around 100 km s^{-1} after the transition. The corresponding SFR occurrence in a set of bins of average solar wind speed is displayed in panel (b) for PSP. Notice that the $\langle V_{\rm SW}\rangle$ here refers to the solar wind speed averaged in each SFR interval. As previously mentioned, SFRs at the PSP occur a little more frequently after the stream interface. The contribution of each SIR to the SFR occurrence at each bin of $\langle V_{\rm SW}\rangle$, however, is different, as shown by the colorbar. Almost all SIRs cover the range $\langle V_{\rm SW}\rangle \in (300, 400)$ km s^{-1}, making this range a broad peak of the SFR counts.

The bottom two panels in Figure 2 show the overview in the same manner for the result at L1 point. Panel (c) now presents the solar wind speed within [−24, 24] hr (centered at the stream interface) because the Wind SIRs are longer than those identified by the PSP. The upstream speed approximately ranges from 300 to 500 km s^{-1}, whereas the downstream speed ranges from 400 to 650 km s^{-1}. The transition from low to high

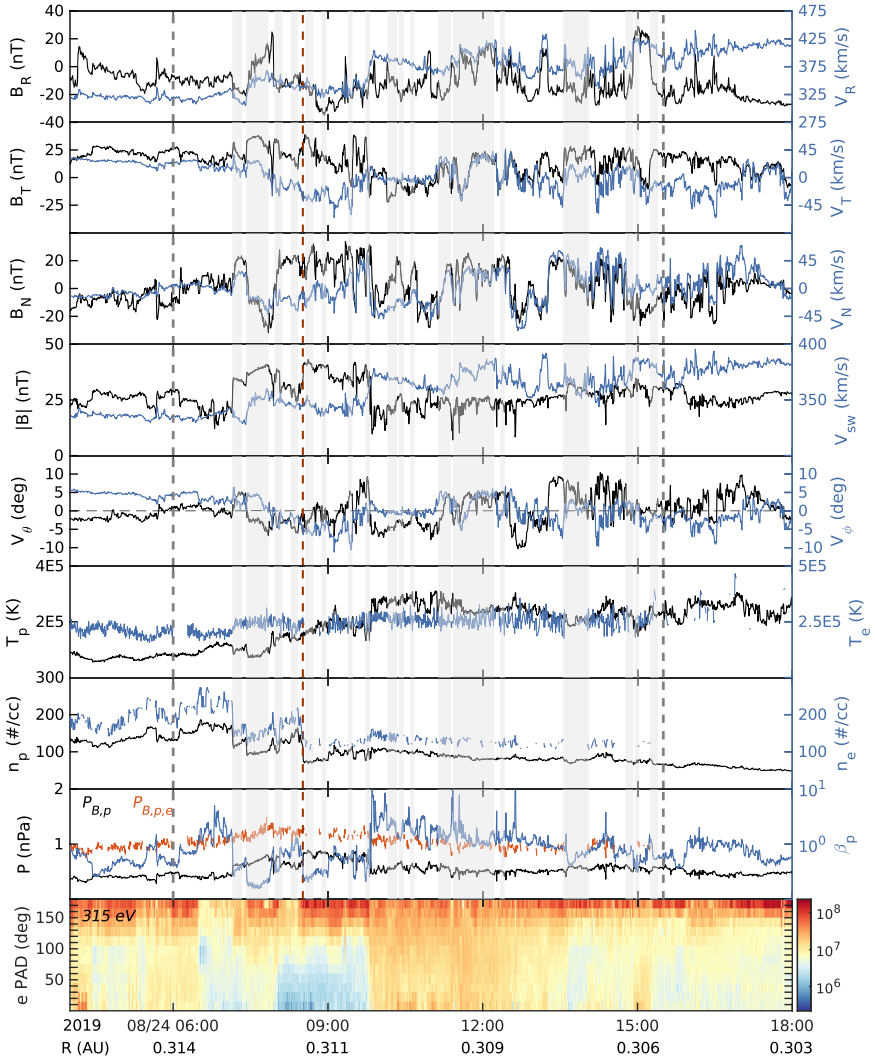

Figure 1. Time-series plot on 2019 August 24, from 04:00 to 18:00 UT, which surrounds the SIR event no. (4) in Table 1. Panels from top to bottom are the magnetic field and solar wind velocity components in the RTN coordinates, the magnitude of magnetic field and the solar wind speed, flow angles V_θ and V_ϕ, the proton temperature T_p and the electron temperature T_e, the proton number density n_p and the electron number density n_e, the total pressure P and the proton β, the ePAD at 315 eV, and the heliocentric distance R. The black and blue colors denote the parameters represented by the left and right y-axes, respectively. The SIR interval and its stream interface are marked by the black and red vertical dashed lines, while the SFR intervals are enclosed by gray shaded areas.

speed is more pronounced at 1 au than at heliocentric distances of less than ∼0.7 au. Panel (d) has a similar tendency to panel (b). SFRs within these intervals occur in different solar wind speed ranges as a result of the varied duration of the SIRs. Also, the SFR occurrence counts tend to peak in a broader range of $\langle V_{\rm SW}\rangle$ than those at PSP.

Figure 3 shows the distributions of selected parameters of SFRs within SIRs from the PSP data set: (a) proton temperature T_p, and (b) proton number density n_p, averaged over each SFR interval. The SFRs are divided into two groups: before and after the stream interface. Although the distributions of the two groups overlap, SFRs still have higher T_p and lower n_p in the presence of relatively high-speed wind, and vice versa. The SFR properties at 1 au such as average T_p and n_p are nearly analogous to the distributions in Figure 3 with more dramatic tendencies. The SFRs with high T_p and low n_p are more common in the high-speed wind (not shown).

We also investigate the number density ratio of the solar wind alpha and proton particles, denoted He/H, whose percentage is also known as the alpha or helium abundance. It is thought to link to solar source regions, and its variations may indicate that the source also changes (Owens et al. 2011). This density ratio has several special ranges. For instance, it is primarily found to be below 5% in the slow to intermediate solar wind at 1 au (Kasper et al. 2007). On the other hand, the enhanced He/H density ratio, such as 0.06, can assist to identify some ICMEs and sometimes help track them from the Sun to the distant places (Richardson et al. 2002; Richardson & Cane 2004). In some sense, this ratio can tell whether an SFR is generated in the solar wind or shares a common feature with an ICME, likely also formed in the low corona (Feng & Wang 2015).

Due to the location of SPAN-Ion instrument being on the ram-facing deck of PSP, the core of the solar wind population is not always within the instrument field of view, particularly when PSP is farther from perihelion (see discussion in Mostafavi et al. 2022). In the meanwhile, there is no publicly available data of alpha particle number density provided by the SPC during these PSP SIR intervals. As a result, we do not present the He/H ratio for the PSP events. Figure 4 shows the distribution of averaged He/H of all SFRs within Wind SIRs in Table 1. At first glance, SFRs after the stream interface have an

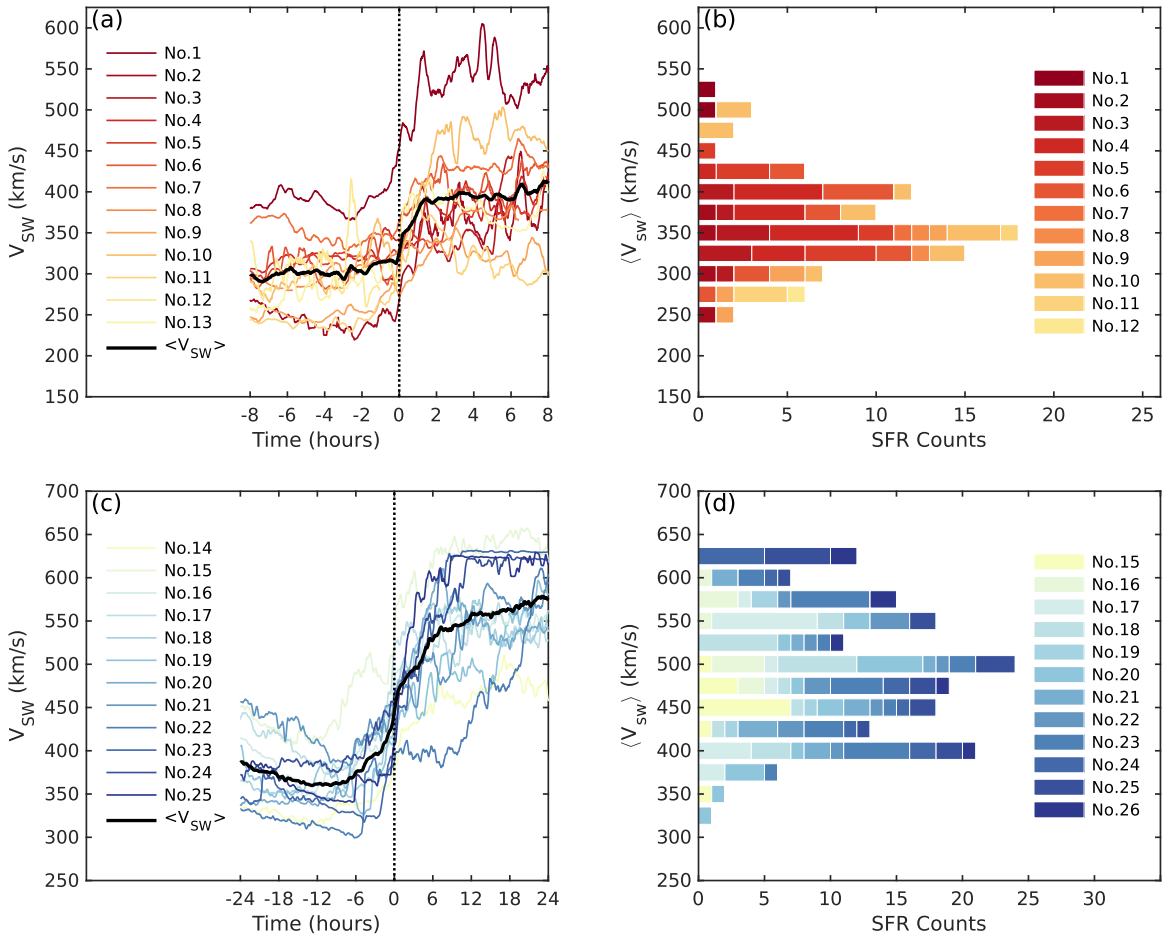

Figure 2. Left column: superposed epoch analyses of solar wind speed (1260 s running average) via the PSP (a) and Wind (c) spacecraft measurements. The average solar wind speed of each panel is denoted by the black curve. Right column: the corresponding stacked distributions of SFR occurrence counts binned by the average solar wind speed, and separated for all SIR events, as indicated by the color bars.

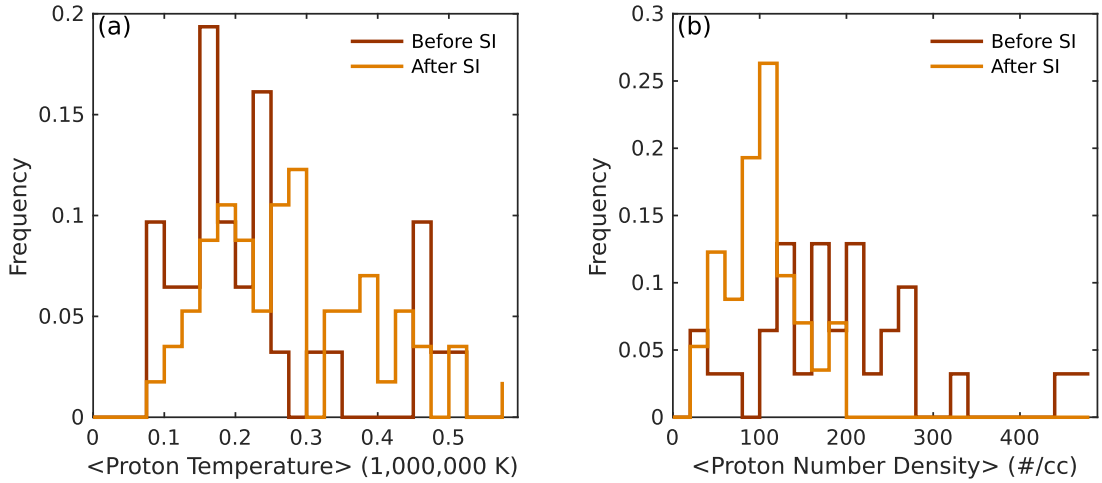

Figure 3. Distributions of SFR properties for events before and after the stream interface from the PSP spacecraft data set: (a) the average proton temperature, and (b) the average proton number density.

obvious peak around 5%, whereas those before it seem to peak at smaller He/H ratio. If we consider the percentages of SFRs possessing He/H density ratios below and above 5%, separately, they are 76.1% versus 23.9% in upstream, and 46.7% versus 53.3% in downstream. These percentages indicate that after the stream interface the SFRs are more likely to have He/H exceeded 5%, which is also consistent with the suggestion in Crooker et al. (1999) that He/H ratio jumps upon crossing the stream interface.

Investigations on the evolution and variation of solar wind structures with heliocentric distance are also worthwhile looking into. Here, we compare the Alfvénicity in the SFRs at different distances. Figure 5 shows two distributions of the absolute values of the Walén test slope. As demonstrated in

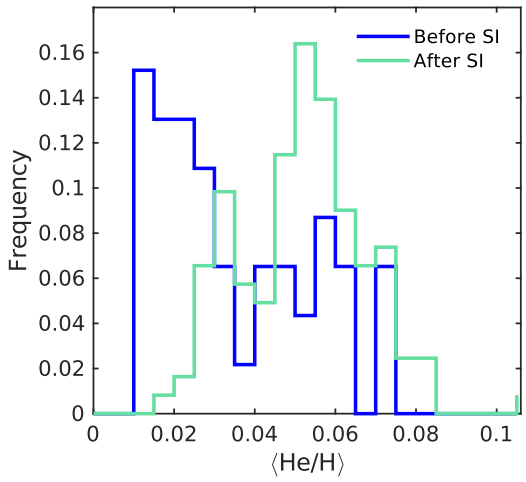

Figure 4. Distribution of the alpha-to-proton number density ratio of SFRs before and after the stream interface from the Wind spacecraft data set.

Figure 5(a), SFRs within PSP SIRs before and after the stream interface all preserve distinct degrees of Alfvénicity, which spans from 0 to 1, i.e., low to high degrees. It is expected that the number of Alfvénic SFRs will be significantly more than the static structures based on our previous investigations of a large sample of events (Chen et al. 2021). Figure 5(b) shows the distribution of the same parameter at L1. Compared with the PSP result, the Alfvénicity of both groups of SFRs decreases noticeably. For example, the peaks of the Walén test slope in the SFRs before and after the stream interface at L1 all decrease to the range [0.05, 0.3]. In fact, 52 out of 168 SFRs identified by the Wind spacecraft have absolute values greater than 0.3, which means that they contain moderate to high Alfvénicity. Such a number becomes 18 (out of 168) if we regard 0.5 as the threshold for highly Alfvénic structure. While for PSP, these numbers are 24/88 and 43/88 when thresholds are 0.3 and 0.5, respectively.

Figure 6 presents the measurements of Alfvénicity at two distances in a separate way. The y-axis of each panel is the normalized residual energy σ_r, which is calculated by $\sigma_r = (\langle v^2\rangle - \langle b^2\rangle)/(\langle v^2\rangle + \langle b^2\rangle)$. The x-axis is the product of the sign of the radial magnetic field, and the normalized cross helicity $\sigma_c = 2\langle v\cdot b\rangle/(\langle v^2\rangle + \langle b^2\rangle)$. We apply the product in accordance with the findings in Chen & Hu (2022), i.e., whether the structure identified by the PSP propagates outward depends on the signs of both the radial magnetic field and σ_c. As shown in Figure 6, the σ_c of SFRs via both the PSP and Wind scatters in a wide range from -1 to 1, with the majority of events clustering around the negative values, indicating mostly outward propagating. The σ_r values are also in the negative range, but have different magnitudes. Theoretically, the pure Alfvén wave is supposed to have $\sigma_r = 0$, and $\sigma_c = \pm 1$ (Bruno & Carbone 2013). Most SFRs at Wind thus cannot be characterized as strongly Alfvénic structures due to relatively significant σ_r values. We also notice that modest to high values of σ_c are from PSP SFRs in almost all ranges of solar wind speeds. To put it another way, the degree of Alfvénicity in SFR does not depend on the solar wind speed. This tendency is consistent with the findings that predominant Alfvénic structures can be found in both the fast-speed wind at high latitudes and the slow solar wind close to the Sun (McComas et al. 2003; Bale et al. 2019; Kasper et al. 2019).

4. SFRs in SIRs from the Same Solar Sources

As mentioned in the beginning, some SIRs are essentially considered to be CIRs since they last longer than one entire solar rotation. Such events, with the slow and fast solar wind streams coming from relatively long-lived (with respect to solar rotation cycle) sources, can be detected by multiple spacecraft and sometimes multiple times. In the following analysis, there are five such corresponding SIRs in Allen et al. (2021) listed by their occurring times in Table 1: Wind SIRs nos. (14), (16), (18), (20), and PSP SIR no. (1). They are also marked as HCS-associated events in Allen et al. (2021). According to the ePAD data via the Wind spacecraft measurements, HCS crossings are generally several days before SIRs.

Figure 7 displays the superposed epoch analysis of solar wind speed of the aforementioned five recurring SIR events. The upstream speeds for all 5 events are rather consistently ranging from ~300 to 450 km s^{-1}. For the downstream speeds, they continuously increase to a range between 400 and ~600 km s^{-1}. Notice that this analysis is implemented within [−24, 24] hr centered on the stream interface, which may thus be longer than the corresponding SIR intervals. For example, the leading part of Wind event no. (16) (<−18 hr) has a decrease of upstream speed. This part, in reality, is beyond the SIR interval, while the actual start of this event is −12 hr. SFR intervals in each SIR are denoted by shaded areas in the corresponding event colors. They tend to occur more frequently in the relatively high-speed solar wind after the stream interface. As previously mentioned, an SFR is suspected to occur with the corresponding SIRs repeatedly. In order to separate from the SIR sequence number, those SFR intervals are marked by Roman numerals (I), (II), and (III). The first SFR (I) takes place immediately following the stream interface, while the second and third SFRs are upstream events before the corresponding stream interfaces. In Figure 7, they are also highlighted by rectangles with the dashed lines, whose colors correspond to the legends of Wind SIR nos. (14), (16), and (20) (see also Table 2), respectively. More information and the temporal variations will be presented in the following two subsections, and the related observations at the PSP are discussed in the third subsection.

4.1. Overview of SFRs in Recurring SIRs at 1 au

Figures 8 and 9 present the time-series variations for the aforementioned SIR events at 1 au: Wind nos. (14), (16), (18), and (20), as indicated by the titles. In each subfigure, the first panel shows the three components of the magnetic field as well as its magnitude. They are given in the geocentric solar ecliptic (GSE) coordinates, and the three components (X, Y, Z) are represented by the red, green, and blue colors, respectively. The SIR interval and the stream interface are marked by vertical dashed lines in black and red, respectively, whereas the SFRs are enclosed by shaded areas (including blue regions that will be discussed in Section 4.2). In order to better understand the evolution of the Alfvénicity, we also calculate fluctuations of solar wind and Alfvén velocities, which is derived from a 10 minutes sliding window analysis. The correlation coefficients between δV and δV_A after averaging three components within these two SIR intervals are −0.37 and 0.29, respectively. Such numbers indicate that these intervals seldom have high correlations, i.e., rather exhibiting low Alfvénicity, except for some shorter time periods. In other words, simultaneous

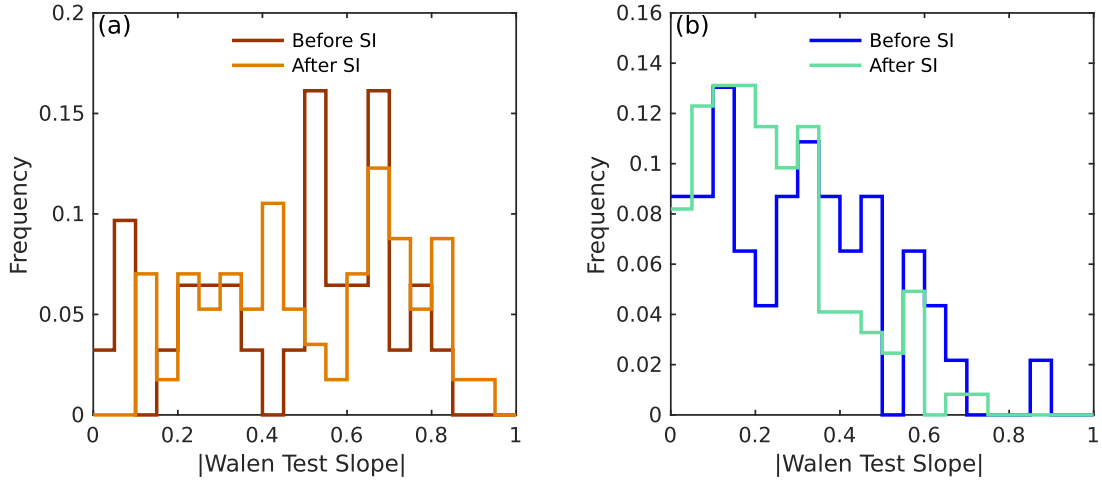

Figure 5. Distributions of the absolute values of the Walén test slopes of SFRs before and after the stream interface from (a) PSP, and (b) Wind spacecraft.

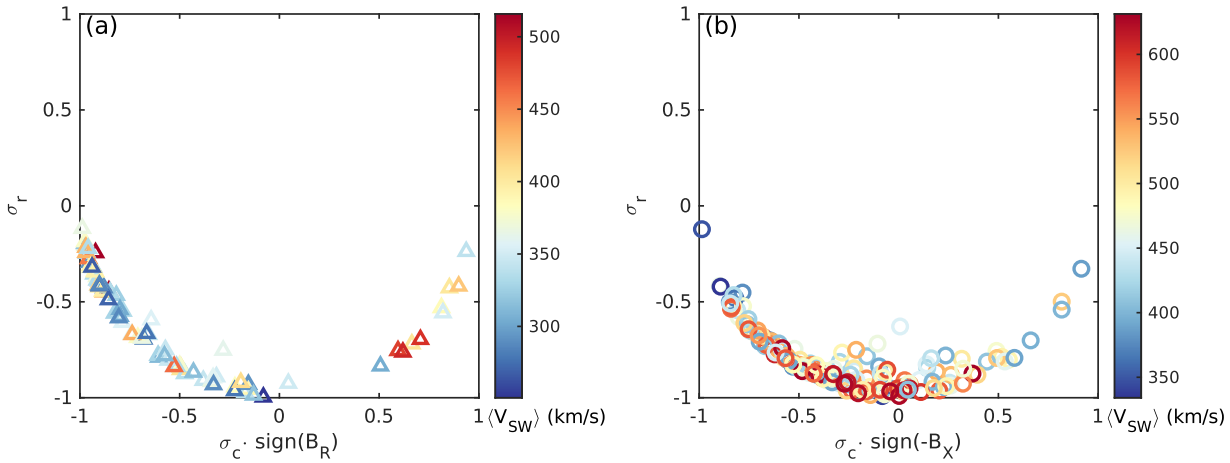

Figure 6. Distribution of the product of sign of radial magnetic field and normalized cross helicity vs. residual energy of SFRs via (a) PSP and (b) Wind.

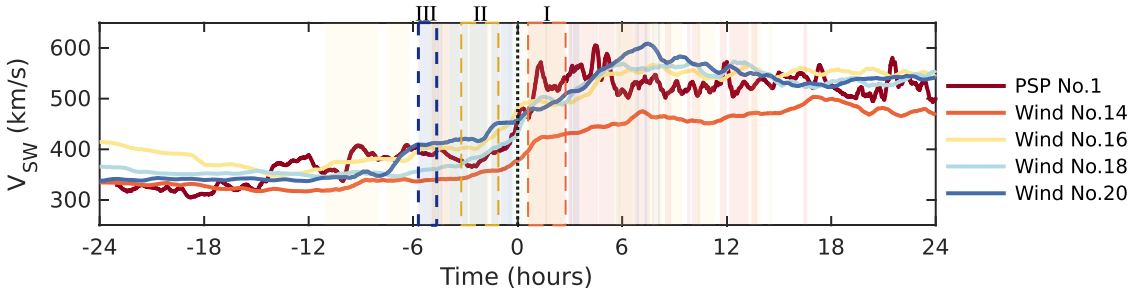

Figure 7. Superposed epoch analysis of solar wind speed for five corresponding SIRs. The central dotted line indicates the time for the stream interface. SFR intervals in each SIR are marked by shaded areas with the corresponding colors shown in the legend. SFRs for case studies are demarcated by additional dashed and solid rectangles.

Table 2
Possibly Recurring SFRs in the Corresponding SIRs

#	Time Periods for the GS-type Reconstruction	$\langle T_p \rangle$ (10^6 K)	$\langle n_p \rangle$ (#/cc)	$\langle$He/H$\rangle$ (%)	Max B_z (nT)	Max j_z (A m^{-2})	Toroidal Flux (Wb)	Poloidal Flux[a] (Wb)
I	2018 Aug 15, 08:16–09:21	0.16	11.66	5.34	5.82	1.90×10^{-11}	4.86×10^{9}	1.96×10^{11}
II	2018 Sep 10, 18:17–19:25	0.13	19.01	4.92	12.05	7.26×10^{-11}	6.88×10^{9}	2.75×10^{11}
III	2018 Nov 4, 16:44–17:39	0.11	12.27	5.57	10.37	1.01×10^{-10}	1.64×10^{9}	1.33×10^{11}

Note.
[a] The poloidal flux is calculated by assuming that the axial length is 1 au.

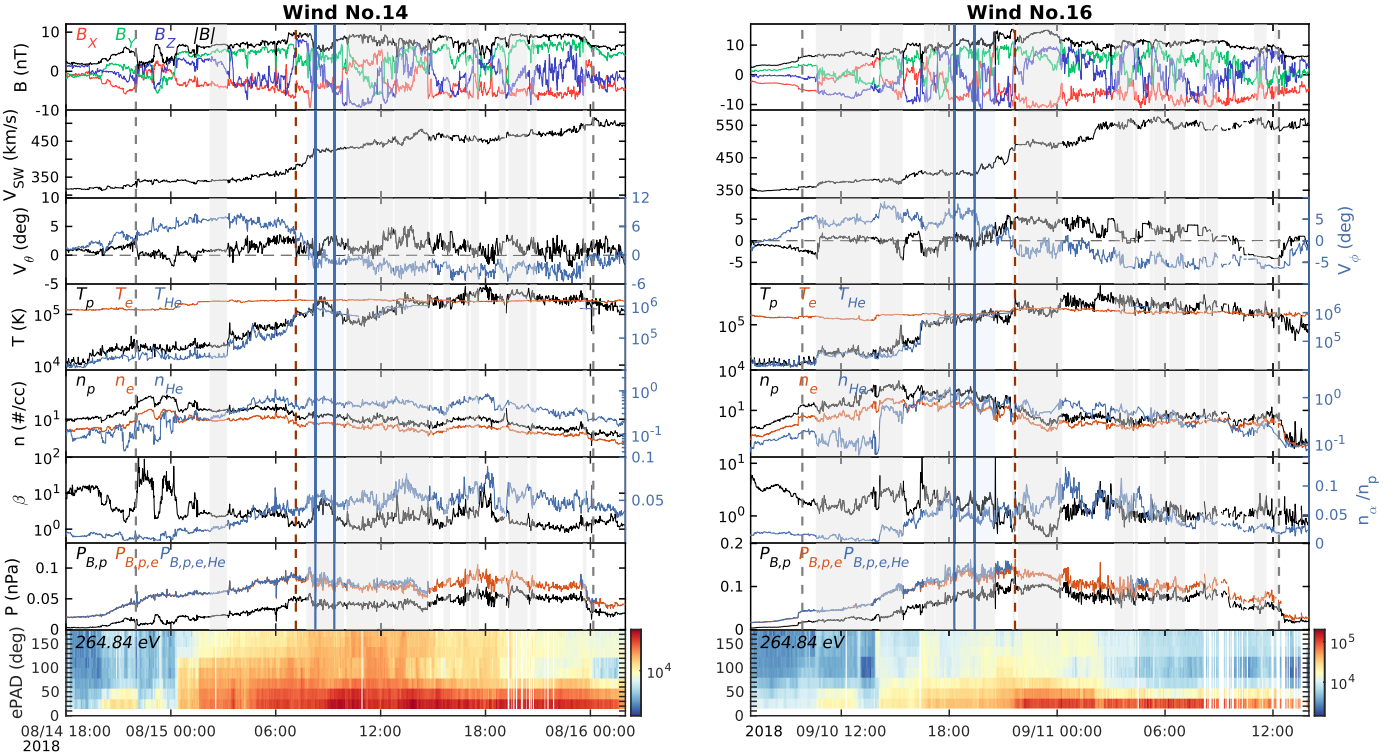

Figure 8. Time-series overview for five corresponding SIRs: Wind no. (14) (left) and Wind no. (16) (right). Panels from the top to bottom for each event are: magnitude of the magnetic field and its three components of in GSE coordinates (red, green, blue), solar wind speed V_{sw}, flow angles V_θ and V_ϕ, T and n (see legends), plasma β and density ratio of He/H, total pressure P, and ePAD at 264.84 eV. The colors black and blue denote the parameters on the left and right y-axes, respectively. The vertical dashed black and red lines mark the SIR intervals and stream interface, whereas SFR intervals are enclosed by shaded areas.

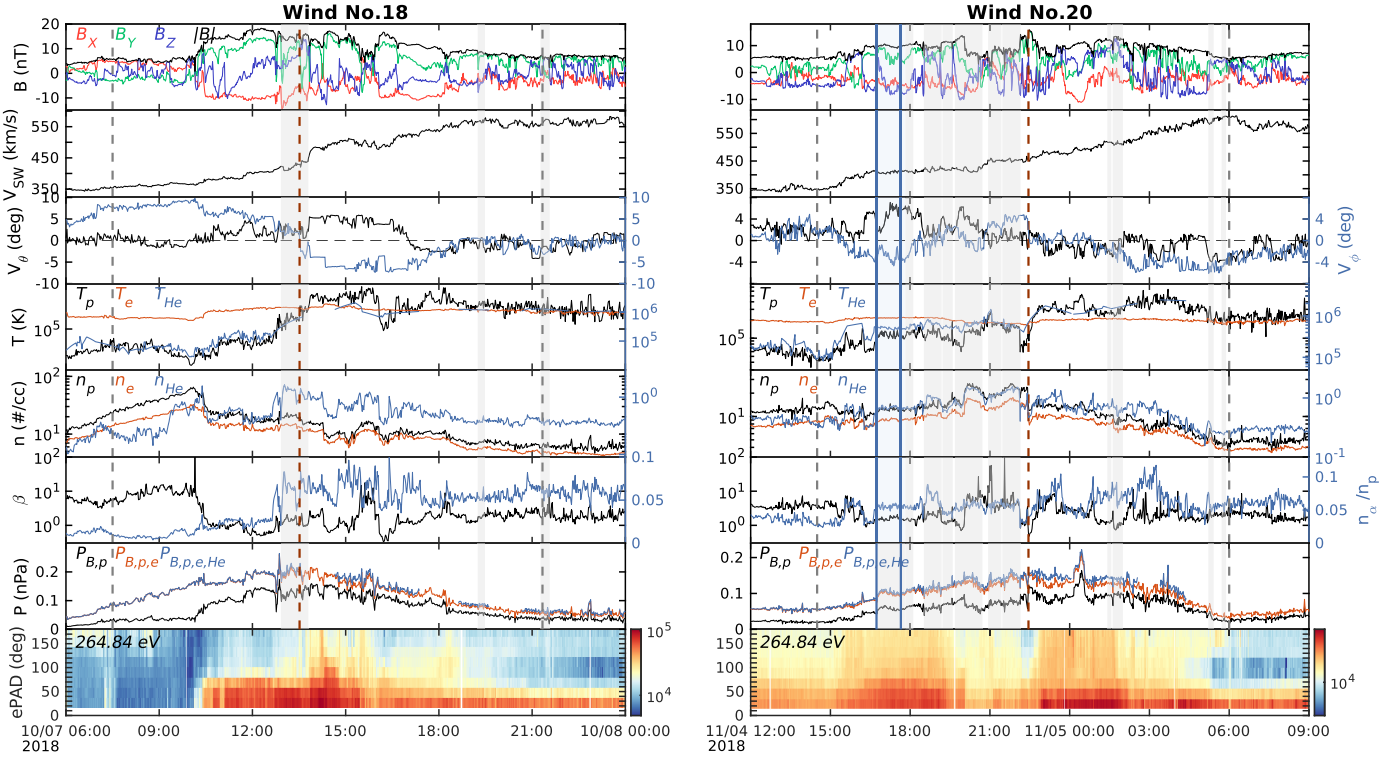

Figure 9. Time-series overview for five corresponding SIRs: Wind no. (18) (left) and Wind no. (20) (right). The format is the same as that of Figure 8.

rotations of solar wind velocity with the magnetic field for these SIR time periods are not significant at 1 au, including the SFR intervals embedded within SIRs.

In the second and third panels, the solar wind speed and flow angles V_θ and V_ϕ (in GSE) are displayed, which have obvious changes when crossing stream interfaces (see also Figure 7).

The fourth to sixth panels present parameters associated with plasma properties, including T, n, and plasma β. The first two parameters, sometimes for all three species (see legends in each panel), have obvious peaks within the whole SIR interval that alternate between n and T. These peaks respond to low- and high-speed solar winds from upstream to downstream. The cross points of transitions between two peaks are sometimes in the vicinity of the time of maximum pressure and also near the stream interface. Notice that $T_{\rm He}$ is discontinuous, and n_e is not approximately identical to n_p during these four SIR intervals. Thus, the plasma β and the total pressure are calculated by substituting $(n_p + 2n_{\rm He})$ for n_e. The plasma β fluctuates a lot and ranges from 0.01 to 10. Some SFRs exhibit stronger proton temperature peaks than their surroundings, which also results in peaks in plasma β. The majority of SFRs, however, still have β values around 1, and neither T_p nor n_p shows unified change. Actually there are some data gaps in n_p and T_p in Wind SIR no. (18) after removing suspected spikes and dramatic fluctuations (not shown), which could be the main reason why the count rate of SFR in this event differs from the others. Both parameters are necessary for calculating the transverse pressure P_t', and n_p is needed for $M_{\rm A}$, based on which the double-folding pattern can be examined.

The number density ratio between the alpha and proton particles is also illustrated in the sixth panel. The alpha particle density $n_{\rm He}$ (not shown) is occasionally compressed after the SIRs start, but consistent changes with n_p before and after the stream interface do not always manifest. The density ratio He/H varies per SIR event. The general tendency rises a little bit toward the stream interface and sometimes has sudden jumps near or at it, e.g., for Wind SIRs nos. (16), (18), and (20). These abrupt changes in the He/H density ratio again demonstrate that the slow and fast solar winds come from different source regions. The peaks of He/H in SIR intervals are also the maxima over longer time periods, which include quiet slow solar wind before the SIR and the following fast-speed wind after the SIR. On the contrary, the depletion of He/H density ratio, i.e., He/H < 0.02, also occurs before or in the compressed slow solar wind. Such a depletion was suggested to be probably caused by the magnetic mirror effect that influences the particle populations through the deflection (Ďurovcová et al. 2019). During the solar minimum, the alpha abundance depletion is also found to occur at one side of the current sheet, as a result of the shear due to different flows of streamer Suess et al. (2009). The latter finding also appears to apply in this study, which has the depletion of He/H around the beginning of the Wind SIR no. (16) in the vicinity of the HCS (also in the solar minimum). Totally, 33 out of 45 SFRs in these five SIRs have He/H ratios greater than 5%. As aforementioned, this signature of significant helium abundance is usually considered as one of the ICME signatures. Therefore, it may suggest that these SFRs share the same source of origin or mechanisms with those large-scale structures.

The seventh panel presents the total pressure, in which the thermal pressure includes contributions from different particles (see legends). In general, the proton and electron data have better coverage than alpha particles. Three pressure values have similar overall tendencies, and the maxima of the total pressure are located at the close points. The last panels in Figures 8 and 9 show the pitch angle distribution of suprathermal electrons at 264.84 eV. Through the ePAD, we find that the enhancement of electron fluxes, sometimes in all angles, is fairly clear within SIR intervals. This behavior differs from that of the suprathermal ions as reported in Allen et al. (2021), which shows the enhancement of suprathermal ions following the streaming interface is weak or not visible at L1 for this event. There is no shock observation earlier to these time periods. Thus, other mechanisms must be responsible for such enhancements. For example, Crooker et al. (2010) found that electron flux peaks around or right at the stream interface by investigating SIRs also via the Wind observation. The interplanetary dynamics associated with compression and/or the coronal hole boundary were considered to be the cause of such concurrence. Some SFRs in Wind SIRs nos. (14), (18), and (20) display unidirectional electron strahls, while some events appear to have diffusive distribution. This is consistent with the statistical results at 1 au, which reports that only one-fifth of SFRs in SIRs exhibit bidirectional enhanced electron fluxes (Xu et al. 2020).

4.2. Case Studies for Temporal Variations of SFRs

Because these five SIRs come from the same solar source and are encountered several times at 1 au, we expect to explore the *same or neighboring* SFRs in each round of in situ measurements. Based on the variations of the magnetic field components, we estimate that the Wind spacecraft may have traversed a recurring SFR several times. They are marked as events (I), (II), and (III) in Figure 7 and enclosed by blue shaded areas in Figures 8 and 9.

The first event occurs on 2018 August 15, from 07:45 to 09:54 UT, immediately following the stream interface of the Wind SIR no. (14). Events (II) and (III) are on 2018 September 10, from 07:45 to 09:54 UT and 2018 November 4, from 16:45 to 17:48 UT, respectively. Both are identified before the stream interfaces. As aforementioned, these SFR intervals are obtained using the GS-based automated detection that adheres to rigorous search criteria. The first two SFRs are initially detected with very similar flux rope z-axes with the principal component in the GSE-Y direction, while event (III) has a distinct z-axis orientation. In the meantime, one should note that certain variations of the magnetic field components during the initial SFR intervals are comparable to one another, but they also have additional portions that are distinct from each other. Since the reconstruction can be implemented independently, we adjust the boundaries of these SFRs to present the structure that shows similar variations. These new boundaries, i.e., 2018 August 15, 08:16 to 09:21 UT, September 10, 18:17 to 19:25 UT, and November 4, 16:44 to 17:39 UT, are marked by blue vertical solid lines in Figures 8 and 9. Moreover, the electron temperature is also included in the GS-type reconstruction when calculating the thermal pressure in Equation (1).

Figure 10 presents the cross-sectional maps of these three SFRs in the first panel and time-series plots in the bottom five panels. The average values of plasma bulk properties and outputs from the GS-type reconstruction are listed in Table 2. In Figure 10, one can see that the B_Z component of three SFRs gradually shifts from the positive to negative values, although to different extents. B_X and B_Y show moderate changes and remain positive and negative separately. All cross sections of these SFRs clearly show the closed field lines of the transverse field B_t (black curves) and unipolar axial field B_z (color background), confirming the SFR signatures with right-handed chirality. The region within the white curve is reconstructed from the spacecraft data, while the region outside the white

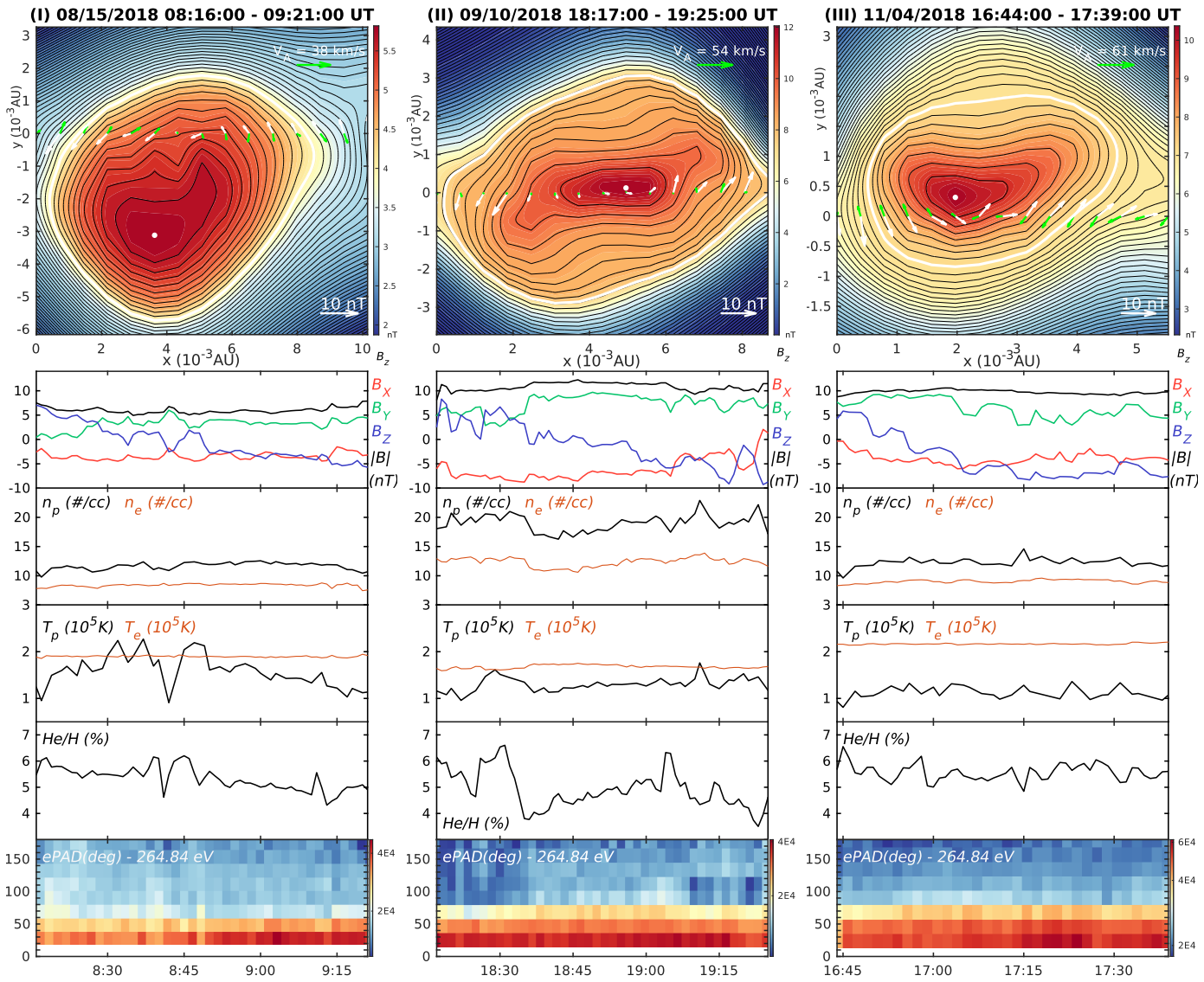

Figure 10. The GS-type reconstruction results (top panel) and time-series variations (the bottom five panels) for SFRs in Table 2: (I) 2018 August 15, 08:16 to 09:21 UT with $\hat{z} = [-0.41, 0.9, -0.13]$, (II) 2018 September 10, 18:17 to 19:25 UT with $\hat{z} = [-0.70, 0.70, -0.09]$, and (III) 2018 November 4, 16:44 to 17:39 UT with $\hat{z} = [-0.77, 0.57, -0.29]$ in the GSE coordinate at Wind spacecraft. The colored background represents the axial field B_z (as indicated by the colorbar) with its maximum value denoted by the white dot, whereas the black curves display the transverse field B_t. Two sets of vectors along the $y = 0$ indicate the remaining flow (green) and B_t (white) along the spacecraft path. The average V_A during this time period is denoted in the top right. The white curve encloses the reconstructed area from the spacecraft measurements, while the outside region is reconstructed via extrapolation. Panels in time-series plots include magnetic field B_X, B_Y, B_Z (in GSE), and its magnitude, n_p and n_e and T_p and T_e, alpha-to-proton density ratio He/H, and ePAD at 264.84 eV.

curve is from extrapolation. Along the spacecraft path ($y = 0$), the correlations between the transverse remaining flow (green vectors) and B_t (white vectors) are different. The remaining flow vectors are small compared with the Alfvén speed in the event (II), while they become more significant in magnitude and appear antiparallel to B_t in the first and third SFR intervals. As a result, the Walén test slopes are −0.32, 0.17, and −0.46, which suggests that three SFRs have different levels of Alfvénicity. Event (II) is a quasi-static structure, while the events (I) and (III) correspond to moderately Alfvénic structures. The maximum B_z is denoted by the white dot near the center of each flux rope. Such values for the three SFRs are 5.82, 12.05, and 10.37 nT, respectively (see also Table 2). The maximum axial current density j_z, which is derived from the GS equation, also has different values.

The second to fourth panels in time-series plots of Figure 10 show the corresponding plasma parameters, such as the temperature, number density, and He/H. Three SFRs have distinct proton number densities but similar temperatures, with the average values also shown in Table 2. This is because they are located at different places relative to stream interfaces and have different solar wind speeds, although SFRs (II) and (III) are both upstream events (see Figures 8 and 9). As aforementioned, event (I) is a downstream event in the relatively high-speed solar wind. Thus, its average number density is a little smaller than the other two events, while the average temperature is the largest of these three SFRs. Event (II) is detected on the way to the apex of T_p, while the n_p starts to pile up already. Event (III) is detected when both T_p and n_p are still growing. The average density ratios of He/H for these

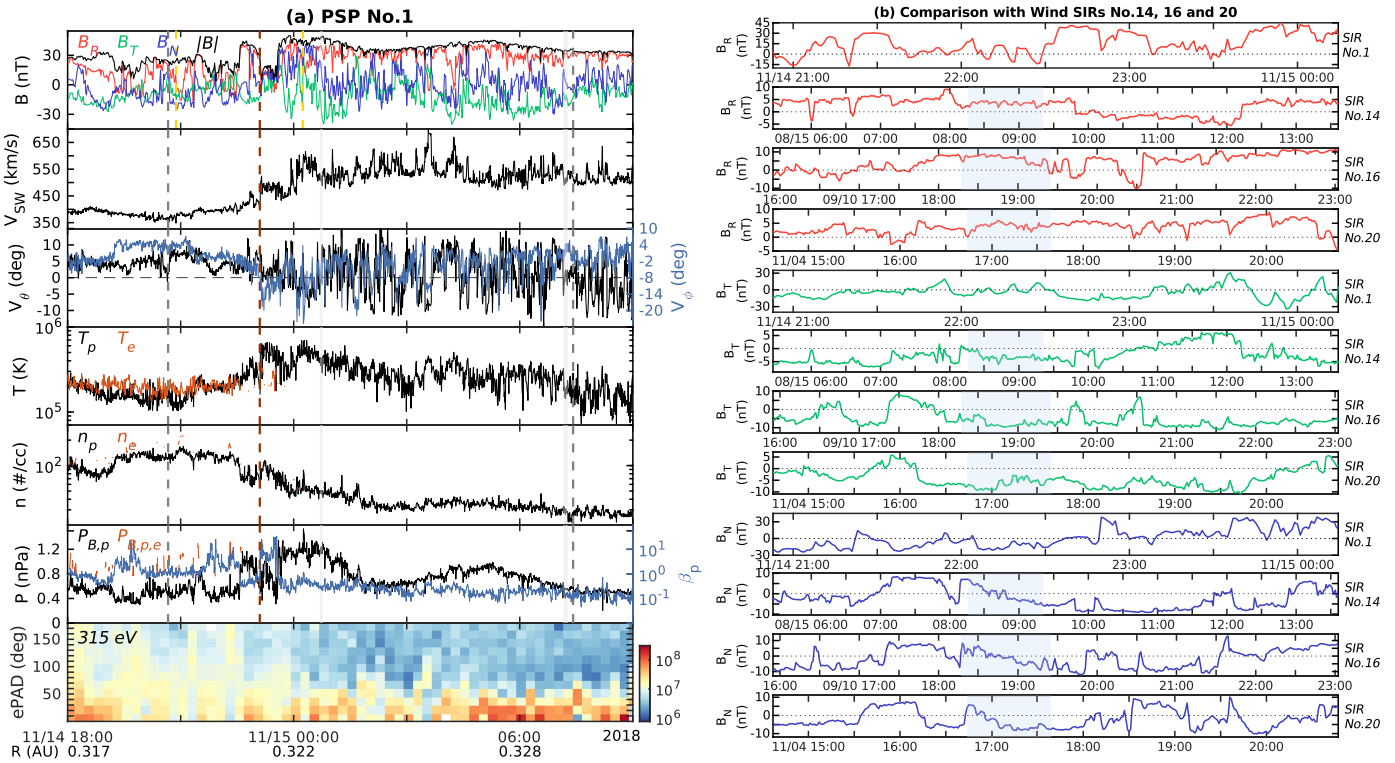

Figure 11. Time-series overview for five corresponding SIRs: (a) PSP no. (1) (see Table 1). The format is the same as the Figure 8, except that the magnetic field and velocity are in the RTN coordinates, the proton β and the total pressure are plotted together in the sixth panel, and the ePAD is at 315 eV. Panel (b) provides the zoomed-in view of the magnetic field between two yellow dashed–dotted lines in (a), i.e., 2018 November 14, 20:52:48 to November 15, 00:14:33 UT, as well as the corresponding Wind spacecraft measurements in RTN coordinates within the time intervals of SIRs nos. (14), (16), and (20).

events are 5.34%, 4.92%, and 5.57%, respectively. These high-density ratios could suggest the similarity to ICME and thus imply a connection to the source in the corona. In general, the pitch angle distribution of suprathermal electrons is another feature that can help specify the source of origin. Within these event intervals, the electron strahls are mostly unidirectional, which possibly signifies that these SFRs, if with closed magnetic field lines rooted on the solar surface in the beginning, may reconnect with open field lines at one footpoint (see also Rouillard et al. 2009). The last two columns in Table 2 list the toroidal (axial) and poloidal magnetic fluxes, which are derived from the GS-type reconstruction. The poloidal magnetic flux per unit length is an output from the GS reconstruction, and the poloidal flux is calculated assuming that the axial length is 1 au (see Hu 2017 for more details). Both the poloidal and toroidal magnetic fluxes of these three events have the same orders of magnitude and are comparable.

Recalling the aforementioned similarities among SFRs (I), (II), and (III), we believe that these three events, especially the last two, are recurring structures in the corresponding SIRs and detected each time by the Wind spacecraft. All magnetic configurations affirm the signatures of SFR at 1 au, despite the fact that the remaining plasma flows have varying degrees of correlation with the magnetic field. Starting from event (I), one may imagine that an SFR carries a significant amount of magnetic flux, travels with the relatively fast solar wind stream, possesses unidirectional suprathermal electrons, retains the proper He/H density ratio, and thus maintains the linkage to the solar source until it is first observed by the Wind spacecraft. After one solar rotation, it may experience changes in footpoint locations to a source of slow solar wind and was detected again during the second and third rounds. During this transition the similar plasma bulk properties, the 2D magnetic field configurations, and magnetic flux contents are maintained. Moreover, it also maintains the similar high-density ratios of He/H resembling the ICMEs. And the signature of unidirectional suprathermal electrons could relate to the mechanism of the interchange reconnection at the source. Both characteristics indicate the connection with the solar source.

4.3. Recurring SIR at the PSP

As was mentioned, there is a PSP SIR in those five corresponding events, which thus provides us an opportunity to survey the possible radial changes. Figure 11(a) presents the overview of the PSP SIR (no. (1) in Table 1). The magnetic field and solar wind velocity are now in the RTN coordinates, with the three components marked in red, green, and blue, respectively. Compared with the L1 measurements, the magnetic field via the PSP data set is more dynamic with several abrupt changes. Moreover, we also calculate the correlation coefficients between the fluctuations of the Alfvén velocity or the magnetic field and those of the solar wind velocity. The average coefficient for the three components is 0.86, which reveals the highly correlated association in some subintervals inside the SIR. Compared with the aforementioned Wind SIR intervals, one can conclude that the Alfvénicity in terms of the correlation coefficient for the entire event interval drops by a half from ~0.35 to 1 au. What resembles 1 au SIRs is that the T and n have the alternating occurrence of peaks, V_{sw} increases apparently with visible flow deflections, and the proton β is mostly below 1, especially after the stream interface (red dashed line). The last panel shows the ePAD at 315 eV. With the exception of those clear unidirectional electron

strahls, the overall enhancements of electrons as seen within 1 au SIRs do not manifest in this SIR interval at PSP.

Only two SFRs are found within this PSP event interval, which could result from the data gaps in the plasma parameters, especially for the n_p that is required to calculate P_t' and M_A. Thus, it is impossible to draw the statistical conclusion in this corresponding SIR at PSP. Since the GS reconstruction can be implemented independently, we attempted to manually select the plausible intervals during this time period, mainly according to time-series changes in the magnetic field within the SIR event no. (14) at 1 au. For that purpose, we transform the Wind spacecraft measurements to RTN coordinates to compare with the PSP counterparts. A subinterval is selected and emphasized by two vertical dashed–dotted lines in Figure 11(a). Notice that it covers both the upstream and downstream parts. Figure 11(b) provides the zoomed-in views and the corresponding Wind spacecraft observations in SIRs nos. (14), (16), and (20). The colors used for both the Wind and PSP magnetic fields are the same as the first panel of Figure 11(a). Intervals of events (I), (II), and (III) in Table 2 are indicated by the blue areas in the panels of SIRs nos. (14), (16), and (20). Similar changes between PSP SIR no. (1) and Wind SIR no. (14), particularly in the radial direction, can be observed near the beginning and ending of this subinterval. The corresponding variations of magnetic field components in recurring SFRs, however, are not evident as expected. As aforementioned, these SFRs have obvious bipolar rotations in B_N component, while the PSP panel barely exhibits such a change. On the other hand, both B_R and B_T have multiple bipolar signatures, which could represent several individual flux ropes or substructures. Such a result may imply that the PSP did not traverse this event.

5. Summary and Discussion

We report the SFRs in the SIRs from the inner heliosphere ~0.15 to 1 au via the in situ measurements by the PSP and Wind spacecraft. The identification of SFRs uses the automated technique, i.e., the extended GS-based detection algorithm, while the SIR event lists are adopted from Allen et al. (2021) and the updated list from the live online catalog. We present the superposed epoch analyses for the solar wind speed of all SIRs, as well as the SFR occurrence as a function of average solar wind speed. Moreover, we analyze the statistical properties of SFRs within SIRs, such as the distributions of proton number density and temperature. The radial evolution of SFR properties, e.g., the degree of Alfvénicity, from the inner heliosphere to 1 au, was also surveyed. In addition, there are five corresponding SIRs detected by both PSP and Wind spacecraft. The similarities and differences between these events are presented. During these five events, we estimate that a recurring SFR was traversed at least twice by the Wind spacecraft. The case studies of the recurring SFRs are supplied with a table that lists the related parameters, detailed time-series plots, and cross-sectional maps for the recurring SFRs. Based on the PSP observations, we also compare the corresponding interval for these recurring SFRs. The following is a summary of the primary findings.

1. SFRs occur at random sites in SIRs, with more frequent occurrence in downstream solar wind with respect to the stream interface. The transition from upstream to downstream solar wind speed is more dramatic in Wind SIRs than at PSP. The SFR occurrence count thus peaks over a wide range of average solar wind speed at 1 au.
2. The solar wind bulk properties of SFRs respond well to the change in solar wind speed at both distances. In the high-speed solar wind, for example, SFRs tend to have higher proton temperature and lower number density, and vice versa. The distributions of density ratios He/H of SFRs at 1 au show that there are more SFRs with higher He/H ratios occurring in relatively fast solar wind.
3. The variation of Alfvénicity of SFRs within SIRs was illustrated from distributions of the Walén test slopes and the normalized cross helicity as well as the residual energy of each event. The Alfvénicity, as measured by the magnitude of the Walén slope, declines at least by a half from the inner heliosphere to 1 au, especially for the downstream SFRs.
4. Time-series variations of five corresponding SIRs also confirm the above findings. Meanwhile, SIRs from the inner heliosphere to 1 au mostly maintain their signatures, such as the compressed proton number density, increased temperature, and the enhancement of suprathermal electrons. SFRs in these five SIRs do not have consistent changes in field magnitude, proton number density, and temperature.
5. A recurring SFR is conjectured to be traversed by the Wind spacecraft at least twice, embedded within the corresponding SIRs. Each SFR can be reconstructed via similar flux rope z-axes by the GS reconstruction. The variations in the magnetic field are very similar, so are the chirality of the 2D configuration and the amounts of magnetic flux contents with the same order of magnitude (in particular the poloidal component). They also have comparable plasma bulk parameters, such as T_p, n_p, and the He/H density ratio, and also possess signatures of unidirectional suprathermal electrons.

All three SFRs that are speculated to be recurring structures have a linkage to the solar source. As previously stated, the alpha abundance is a typical signature of the solar source, and the high ratio is usually seen in the ICMEs. In the case studies, it shows a moderate density ratio in all three events. In other words, they share a common characteristic with ICMEs, which may thus act as a proxy for assuming a link to the solar source. Furthermore, they also manifest unidirectional suprathermal electrons. Such a phenomenon could result from the interchange reconnection of SFRs, which initially have field lines rooted on the solar surface and may reconnect with the open field lines at one footpoint (Rouillard et al. 2009).

Among these three SFRs, event (I) may be debatable since it takes place right after the stream interface while the other two SFRs are upstream events. Such an inconsistency may be ascribed to the stream interface that was not well formed in the inner heliosphere, and/or SFR propagating into other streams due to random walks of footprints of magnetic field lines or other factors.

Based on those consistencies with the other two events and its close location to the stream interface, it is likely that this SFR is the first structure recurring in the next few solar rotations. In fact, there are three sets of recurring SIRs or CIRs according to Allen et al. (2021). However, the recurring SFRs inside CIRs are still rare. Such a result could be attributed to their smaller scales that may be easily missed by a spacecraft, and the intrinsic variabilities in solar wind streams.

Our analysis of the PSP observation during SIR no. (1) only yields two SFRs, which is thus inadequate to make any statistical conclusion. For the recurring SFR at 1 au, we attempted to visually identify the corresponding interval at the PSP covering similar variations of the magnetic field components. The selected time period manifests multiple bipolar rotations, which could be several flux ropes or substructures. They are likely associated with the interchange reconnection as well due to the appearance of the unidirectional electron strahls. However, the major rotating component is in a different direction from that at 1 au. This inconsistency could imply that this structure was not traversed by the PSP.

Case studies with the spatial changes for widely separated heliocentric distances are limited at this moment, due to the scarce number of events and significant fluctuations in the PSP SIR measurements. Our future work will follow by examining additional SIR events at distances close to the Sun, e.g., from Solar Orbiter, and at ∼1 au. In particular, the multipoint observations from radially aligned spacecraft will provide coordinated measurements for investigating the possible radial evolution of one specific solar wind stream.

We are grateful for the helpful comments and suggestions from the reviewer, which improve and enhance this manuscript. We thank Dr. Robert Livi for providing the instruction on acquiring the PSP SPAN-Ion data set and Dr. Lingling Zhao for discussion about the data processing. Y.C. and Q.H. acknowledge NASA grants 80NSSC19K0276, 80NSSC21K0003, 80NSSC21K1319, 80NSSC21K1763, and NSF award AGS-2229065 for support. R. C.A. acknowledges support from NASA grant 80NSSC21K0733 and NASA contract NNN06AA01C. The PSP and Wind spacecraft data are obtained via the NASA Coordinated Data Analysis Web (CDAWeb[5]). This work was made possible in part by a grant of high-performance computing resources and technical support from the Alabama Supercomputer Authority.

ORCID iDs

Yu Chen https://orcid.org/0000-0002-0065-7622
Qiang Hu https://orcid.org/0000-0002-7570-2301
Robert C. Allen https://orcid.org/0000-0003-2079-5683
Lan K. Jian https://orcid.org/0000-0002-6849-5527

References

Agapitov, O. V., Drake, J. F., Swisdak, M., et al. 2022, ApJ, 925, 213
Allen, R. C., Ho, G. C., Jian, L. K., et al. 2021, A&A, 650, A25
Allen, R. C., Lario, D., Odstrcil, D., et al. 2020, ApJS, 246, 36
Bale, S. D., Badman, S. T., Bonnell, J. W., et al. 2019, Natur, 576, 237
Bale, S. D., Goetz, K., Harvey, P. R., et al. 2016, SSRv, 204, 49
Borovsky, J. E. 2008, JGRA, 113, A08110
Bruno, R., & Carbone, V. 2013, LRSP, 10, 2
Cartwright, M. L., & Moldwin, M. B. 2010, JGR, 115, A08102
Case, A. W., Kasper, J. C., Stevens, M. L., et al. 2020, ApJS, 246, 43
Chen, Y., & Hu, Q. 2020, ApJ, 894, 25
Chen, Y., & Hu, Q. 2022, ApJ, 924, 43
Chen, Y., Hu, Q., & le Roux, J. A. 2019, ApJ, 881, 58
Chen, Y., Hu, Q., Zhao, L., Kasper, J. C., & Huang, J. 2021, ApJ, 914, 108
Chi, Y., Shen, C., Luo, B., Wang, Y., & Xu, M. 2018, SpWea, 16, 1960
Cohen, C. M. S., Christian, E. R., Cummings, A. C., et al. 2020, ApJS, 246, 20
Crooker, N. U., Appleton, E. M., Schwadron, N. A., & Owens, M. J. 2010, JGR, 115, A11101
Crooker, N. U., Gosling, J. T., Bothmer, V., et al. 1999, SSRv, 89, 179
Drake, J., Agapitov, O., Swisdak, M., et al. 2021, A&A, 650, A2
Ďurovcová, T., Němeček, Z., & Šafránková, J. 2019, ApJ, 873, 24
Feng, H. Q., & Wang, J. M. 2015, ApJ, 809, 112
Finley, A. J., McManus, M. D., Matt, S. P., et al. 2021, A&A, 650, A17
Gosling, J. T. 1990, Coronal Mass Ejections and Magnetic Flux Ropes in Interplanetary Space (Washington, DC: American Geophysical Union), 343
Greco, A., Matthaeus, W. H., Servidio, S., Chuychai, P., & Dmitruk, P. 2009, ApJL, 691, L111
Hau, L.-N., & Sonnerup, B. U. Ö. 1999, JGR, 104, 6899
Hu, Q. 2017, ScChD, 60, 1466
Hu, Q., & Sonnerup, B. U. Ö. 2002, JGR, 107, 1142
Hu, Q., Zheng, J., Chen, Y., le Roux, J., & Zhao, L. 2018, ApJS, 239, 12
Jian, L., Russell, C. T., Luhmann, J. G., & Skoug, R. M. 2006, SoPh, 239, 337
Jian, L. K., Luhmann, J. G., Russell, C. T., & Galvin, A. B. 2019, SoPh, 294, 1
Jian, L. K., Russell, C. T., Luhmann, J. G., Galvin, A. B., & MacNeice, P. J. 2009, SoPh, 259, 345
Jian, L. K., Russell, C. T., Luhmann, J. G., Galvin, A. B., & Simunac, K. D. C. 2013, in AIP Conf. Proc. 1539, Solar Wind 13, ed. G. P. Zank et al. (Melville, NY: AIP), 191
Kasper, J. C., Abiad, R., Austin, G., et al. 2016, SSRv, 204, 131
Kasper, J. C., Bale, S. D., Belcher, J. W., et al. 2019, Natur, 576, 228
Kasper, J. C., Stevens, M. L., Lazarus, A. J., Steinberg, J. T., & Ogilvie, K. 2007, ApJ, 660, 901
Kilpua, E. K. J., Luhmann, J. G., Gosling, J., et al. 2009, SoPh, 256, 327
Lepping, R. P., Acũna, M. H., Burlaga, L. F., et al. 1995, SSRv, 71, 207
Lin, R. P., Anderson, K. A., Ashford, S., et al. 1995, SSRv, 71, 125
Livi, R., Larson, D. E., Kasper, J. C., et al. 2022, ApJ, 938, 138
McComas, D. J., Elliott, H. A., Schwadron, N. A., et al. 2003, GeoRL, 30, 1517
Moldwin, M. B., Ford, S., Lepping, R., Slavin, J., & Szabo, A. 2000, JGR, 27, 57
Moldwin, M. B., Phillips, J. L., Gosling, J. T., et al. 1995, JGR, 100, 19903
Moncuquet, M., Meyer-Vernet, N., Issautier, K., et al. 2020, ApJS, 246, 44
Mostafavi, P., Allen, R. C., McManus, M. D., et al. 2022, ApJL, 926, L38
Ogilvie, K. W., Chornay, D. J., Fritzenreiter, R. J., et al. 1995, SSRv, 71, 55
Owens, M. J., Wicks, R. T., & Horbury, T. S. 2011, SoPh, 269, 411
Pecora, F., Servidio, S., Greco, A., & Matthaeus, W. 2021, A&A, 650, A20
Richardson, I. G., & Cane, H. V. 2004, JGR, 109, A09104
Richardson, J. D., Paularena, K. I., Wang, C., & Burlaga, L. F. 2002, JGR, 107, 1041
Rouillard, A. P., Savani, N. P., Davies, J. A., et al. 2009, SoPh, 256, 307
Rouillard, A. P., Sheeley, N. R., Cooper, T. J., et al. 2011, ApJ, 734, 7
Smith, E. J., & Wolfe, J. H. 1976, GeoRL, 2, 137
Sonnerup, B. U. Ö., & Guo, M. 1996, GeoRL, 23, 3679
Suess, S. T., Ko, Y.-K., von Steiger, R., & Moore, R. L. 2009, JGR, 114, A04103
Teh, W.-L. 2018, EP&S, 70, 1
Teh, W.-L. 2021, JGR, 126, e2021JA029944
Whittlesey, P. L., Larson, D. E., Kasper, J. C., et al. 2020, ApJS, 246, 74
Xu, M., Shen, C., Hu, Q., Wang, Y., & Chi, Y. 2020, ApJ, 904, 122
Yu, W., Farrugia, C. J., Lugaz, N., et al. 2014, JGR, 119, 689
Zank, G. P., le Roux, J. A., Webb, G. M., Dosch, A., & Khabarova, O. 2014, ApJ, 797, 28
Zhao, L., Zank, G., Hu, Q., et al. 2021, A&A, 650, A12
Zheng, J., & Hu, Q. 2018, ApJL, 852, L23

[5] https://cdaweb.gsfc.nasa.gov/index.html/